


Article

Corrosion Behavior of the AlCoCrFeNi_{2.1} Eutectic High-Entropy Alloy in Chloride-Containing Sulfuric Acid Solutions at Different Temperatures

Longfei Song ^{*}, Wenbin Hu, Xiaowen Zhang, Bokai Liao , Shan Wan, Lei Kang and Xingpeng Guo ^{*}

School of Chemistry and Chemical Engineering, Guangzhou University, Guangzhou 510006, China; wilbur326@163.com (W.H.); zhangxw0222@163.com (X.Z.); bokailiao@gzhu.edu.cn (B.L.); shanwan@gzhu.edu.cn (S.W.); kanglei@gzhu.edu.cn (L.K.)

^{*} Correspondence: songlongfei@gzhu.edu.cn (L.S.); guoxingpeng@gzhu.edu.cn (X.G.)

Abstract: In this work, the influence of temperature on the corrosion behavior of AlCoCrFeNi_{2.1} eutectic high-entropy alloy in a chloride-containing sulfuric acid solution was investigated using electrochemical measurement, X-ray photoelectron spectroscopy, and scanning electron microscopy. Results show that the passive film of AlCoCrFeNi_{2.1} is stable in chloride-containing sulfuric acid solutions at low temperatures, while an unstable film forms on the alloy at high temperatures. Furthermore, temperature changes the proportion of hydroxide and oxide in Fe and Cr, but it has no noticeable effect on Al and Ni, which is a significant factor on the passive behavior. L12 phase exhibits good corrosion resistance at different temperatures. Pitting occurred on B2 phase in the chloride-containing sulfuric acid solution at a low temperature of 5 °C, while pitting and dissolution take place on AlCoCrFeNi_{2.1} in the acid solution at room temperature and above.

Keywords: eutectic high-entropy alloy; corrosion; passive film



Citation: Song, L.; Hu, W.; Zhang, X.; Liao, B.; Wan, S.; Kang, L.; Guo, X.

Corrosion Behavior of the AlCoCrFeNi_{2.1} Eutectic High-Entropy Alloy in Chloride-Containing Sulfuric Acid Solutions at Different Temperatures. *Materials* **2022**, *15*, 4822. <https://doi.org/10.3390/ma15144822>

Academic Editor: Zbigniew Brytan

Received: 20 June 2022

Accepted: 8 July 2022

Published: 11 July 2022

Publisher's Note: MDPI stays neutral with regard to jurisdictional claims in published maps and institutional affiliations.



Copyright: © 2022 by the authors. Licensee MDPI, Basel, Switzerland. This article is an open access article distributed under the terms and conditions of the Creative Commons Attribution (CC BY) license (<https://creativecommons.org/licenses/by/4.0/>).

1. Introduction

The high-entropy alloy (HEA) is a new alloy with more than four main elements. In recent years, HEAs have attracted attention due to their outstanding performance, including superior mechanical properties, abrasion resistance, and corrosion resistance [1,2]. Single-phase body-centered-cubic (BCC) and face-centered-cubic (FCC) HEAs have been the subject of much research over the past decade. Several studies have reported that BCC HEAs possess high strength, while FCC HEAs are highly ductile. According to comprehensive research, it is difficult to achieve both high strength and ductility in single-phase HEAs [3–5]. To further improve the properties of HEA, Lu et al. [6,7] proposed the concept of eutectic high-entropy alloy (EHEA) that combined the strength of BCC HEAs and ductility of FCC HEAs. EHEAs have broad application prospects due to their excellent mechanical properties over a wide temperature range [8–10]. However, EHEA research mainly focuses on mechanical properties, while there are few studies on the corrosion behavior of EHEAs. Consequently, the development and application of the EHEA have been somewhat restricted.

Passivation behavior and local corrosion are the primary research topics on the corrosion of metals with passivation ability [11–14]. The influence of the component elements and microstructure on the corrosion and passivation behavior of other HEAs has been investigated in the past. Yet, there are few reports on the corrosion behavior of the AlCoCrFeNi_{2.1} EHEA. The content of Al, Co, Cr, Fe, and Ni in the EHEA all affect its passivation behavior, which is essential to the corrosion resistance of the EHEA. Alloys with more than 12 at.% Cr content can form a passive film in some solutions [15]. Cr is the primary component of passive films [16,17]. Additionally, some research have reported that Ni, Al, Co, and Fe can also be the constituent elements in passive films [16,18,19]. Shi et al. [20] established that

an increase in Al content reduced the protective ability of the passive film on the surface of the $\text{Al}_x\text{CoCrFeNi}$ HEA in 3.5% NaCl solutions. Chen et al. [21] discovered that the $\text{Cu}_{0.5}\text{NiAlCoCrFeSi}$ HEA was more prone to pitting than 304 stainless steel in chloride solution. Xu et al. [22] demonstrated that Ni was the central element of the passive film on CoCrFeMnNi HEA in sulfuric acid solution. In addition, Chai et al. [23] revealed that the $\text{FeCoNiCr}_{0.5}$ HEA possessed good local corrosion resistance, while the dissolution of the Cr-rich zone in the dendrites was accelerated. Lin et al. [24] asserted that the Al-Ni-rich phase on FCC was the preferential corrosion area in chloride-containing sulfuric acid solutions. Additionally, unique microstructures alter the corrosion behavior of the $\text{AlCoCrFeNi}_{2.1}$ EHEAs, compared to other HEAs. The eutectic structure may lead to the galvanic effect, which making the EHEA face local corrosion risks.

Corrosion is a serious threat to the security of metals, and is a vital issue in the application of new materials. Scholars have conducted much research about the corrosion behavior of HEAs, but studies on EHEA corrosion are relatively rare. It has been reported that HEAs exhibit different corrosion resistance in various corrosive environments. Wang et al. [25] discovered that the $\text{CoCrFeNiMo}_{0.01}$ EHA displayed pseudo-passive behavior in an H_2S -containing environment. Luo et al. [26] found that the pitting corrosion resistance of the interstitial equiatomic CoCrFeMnNi HEA was influenced by carbon content in a Cl-containing solution. Most studies have focused on the corrosion behavior of HEAs at room temperature ($\sim 25^\circ\text{C}$). However, HEAs would be often used in corrosive mediums at different temperatures. Until now, only a few studies have paid attention to the influence of temperature on the corrosion of HEAs in aqueous solutions. For instance, Chou et al. [27] showed that the pitting potential of the $\text{Co}_{1.5}\text{CrFeNi}_{1.5}\text{Ti}_{0.5}\text{Mo}_{0.1}$ HEA changed linearly with the logarithm of chloride concentration at 70°C and 80°C . Moreover, studies on the corrosion behavior of HEAs are usually based on stainless steel. The relationship between corrosion behavior and environmental temperature is an essential topic in the study of stainless steel. Hou et al. [28] considered that the passive film resistance of 316L SS in methyl diethanolamine solution dropped as the solution temperature rose. Cui et al. [29] established that temperature caused a decrease in the protection of passive properties in 2507 super duplex stainless steel by altering the doping concentrations and structure. Lei et al. [30] reported that pitting corrosion on S44660 stainless steel was more likely to occur in bromide solution than in chloride solution at low temperature. The corrosion behavior of EHEA is greatly affected by temperature, as with stainless steel. Therefore, investigating the influence of temperature on the corrosion behavior of the $\text{AlCoCrFeNi}_{2.1}$ EHEA has great significance to the study of the EHEA corrosion mechanism and the choice of its usage scenarios.

In this paper, the corrosion behavior of the $\text{AlCoCrFeNi}_{2.1}$ EHEA in chloride-containing sulfuric acid solution at different temperatures were studied using field emission scanning electron microscopy (FESEM), energy dispersive spectrometry (EDS), electron backscattering diffraction (EBSD), atomic force microscopy (AFM), electrochemical methods, and X-ray photoelectron spectroscopy (XPS). The effects of temperature on the passive and local corrosion mechanism of EHEA were discussed. This work accumulates basic data for the study of corrosion resistance of EHEA and provides for application of $\text{AlCoCrFeNi}_{2.1}$ EHEA in corrosive environment.

2. Materials and Methods $\text{AlCoCrFeNi}_{2.1}$

2.1. Materials and Solution

$\text{AlCoCrFeNi}_{2.1}$ EHEAs were prepared from high-purity metal (99.95%, Al, Co, Cr, Fe, Ni) in a vacuum melting furnace. The EHEAs were re-melted 5 times to ensure homogeneity. The microstructure and chemical composition of the EHEA were analyzed by FESEM (JSM-7001F, JEOL, Tokyo, Japan) and EDS after polishing and etching with aqua regia for 20 s. Figure 1 displays the microstructure of the EHEA. The alloy consists of a lamella area and irregular area, which is consistent with previous literatures [31,32]. Research has reported that the lamellar region of the $\text{AlCoCrFeNi}_{2.1}$ EHEA contained L12

and B2 phase, respectively [33,34]. The crystallographic information of the EHEA was further analyzed by EBSD, and the sample for EBSD was prepared by electrochemical polishing in an electrolyte with perchloric acid and ethanol (1:4). Scanning Kelvin probe force microscopy (SKPFM) enabled the characterizations of the potential differences between various phases. The SKPFM test of the EHEA was examined by atomic force microscopy (AFM) (Bruker Multimode VIII, Bruker, Billerica, MA, USA). The sample for SKPFM, which had dimensions of 10 mm × 10 mm × 2 mm, was ground with SiC paper to 5000 grit, mechanically polished with 2.5 μm and 1.5 μm diamond paste, and then polished with oxide polishing suspension (OPS) solution. The distance between the probe tip and the EHEA surface was 100 nm. The nominal resonance frequency was 75 kHz, and the spring constant was 3 N/m. The corrosion behaviors of the EHEAs were studied in a 0.005 M H₂SO₄ + 0.05 M NaCl solution at several temperatures (5 °C, 25 °C, 40 °C and 60 °C).

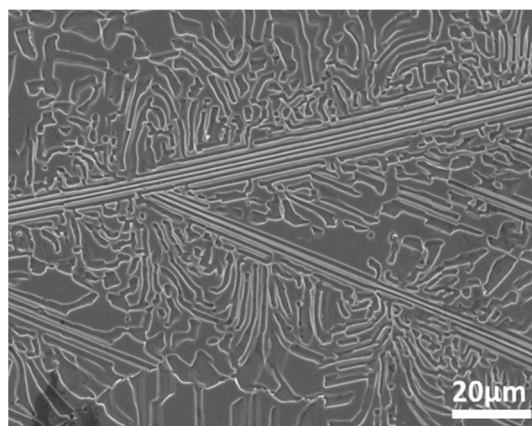


Figure 1. Microstructure of AlCoCrFeNi_{2.1}.

2.2. Electrochemical Tests

The samples for the electrochemical testing methods were embedded in epoxy resin, leaving an exposed area of 1 cm². The working surface was ground with emery paper. In this study, all of the electrochemical tests were carried out on a CHI660 electrochemical workstation (Wuhan, China) using the three-electrode test system. The working electrode, reference electrode, and platinum plate were EHEA, a KCl saturated calomel electrode (SCE), and a counter electrode, respectively. Before all the electrochemical tests, the working electrodes were maintained for 1 h to reach a stable value of the open circuit potential. Potentiodynamic polarization (PDP) curves were measured from −0.3 to 0.6 V_{vs}OCP with a scanning rate of 0.5 mV/s. Electrochemical impedance spectroscopy (EIS) (JSM-7001F, JEOL, Tokyo, Japan) measurements were carried out to study the surface state of the EHEA. During the EIS tests, the testing frequency ranged from 0.01 Hz to 10,000 Hz, and the perturbation amplitude was 10 mV. The EIS data were fitted by ZsimpWin software, (ZSimpWin 3.50 Ann Arbor, MI, USA). Potentiostatic measurements were performed to study the passivation behavior of the EHEAs at different temperatures, and the potential was chosen based on the PDP curve. Mott-Schottky curves were tested from 800 to −600 mV_{vs}SCE with 0.5 V/step at a frequency of 1000 Hz. A fast scan rate was selected to avert a change in the surface state during the tests, which is in accordance with the “frozen-in defect structure”. The electrochemical tests repeated three times to ensure accuracy.

2.3. XPS Tests

To study the passivation behaviors of the EHEAs in chloride-containing sulfuric acid solution at various temperatures, the composition of the film on the EHEA samples after potentiostatic polarization for 4 h at 5 °C and 60 °C was tested by using XPS (AXIS NOVA, SHIMADZU, Kyoto, Japan) equipped with Al K α radiation working at 15 kV and 25 W. The standard peak (C1s, 284.8 eV) was used to correct all the XPS peaks, and the XPS data were analyzed by XPSpeak 4.1 software (freeware written by Raymond Kwok, Hong Kong,

China). The standard peak (C1s, 284.8 eV) was used to correct all the XPS peaks, and the XPS data were analyzed by XPSpeak 4.1 software.

2.4. Corrosion Observation

The surface morphologies of the EHEA after potentiostatic polarization at 0.3 V_{vsSCE} for 20 min were observed using FESEM (JSM-7001F JEOL, Tokyo, Japan), and the element distribution on the corrosion surface was measured by EDS.

3. Results and Discussion

3.1. Microstructure

Electron back-scattering diffraction was used to study the relationship between microstructure and corrosion behavior. Figure 2 shows the EBSD data, including inverse pole figure (IPF), grain, phase, and kernel average misorientation (KAM) map. The EHEA presents three crystal orientations, as Figure 2a illustrates. The volume fractions of FCC and BCC phases were calculated by professional software in the phase map. The volume fraction of the L12 (FCC) phase and the B2 (BCC) phase are 41.2% and 58.8%, respectively. The B2 (BCC) phases (green color) are paralleled in the lamellae area, as shown in Figure 2a. According to the KAM map, the B2 phase possesses a higher KAM value than the L12 phase, indicating that the B2 phase presents a higher dislocation density and, therefore, higher electrochemical activity. The EDS map in Figure 3 shows Al and Ni are enriched in the B2 phase, while FCC is enriched with Cr. SKPFM was used to test the potential of the L12 and B2 phases. Figure 4a,b present the potential map of the lamella region and the eutectic region. It can be seen that there is a definite difference potential between the two phases. The potential of the L12 phase is lower, and the corrosion resistance of the EHEAs is adversely influenced by the galvanic couple effect, which corresponds to the results of EBSD and EDS. In summary, there is a significant difference in the distribution of elements and dislocation between the two phases in the EHEA, resulting in a risk of localized corrosion.

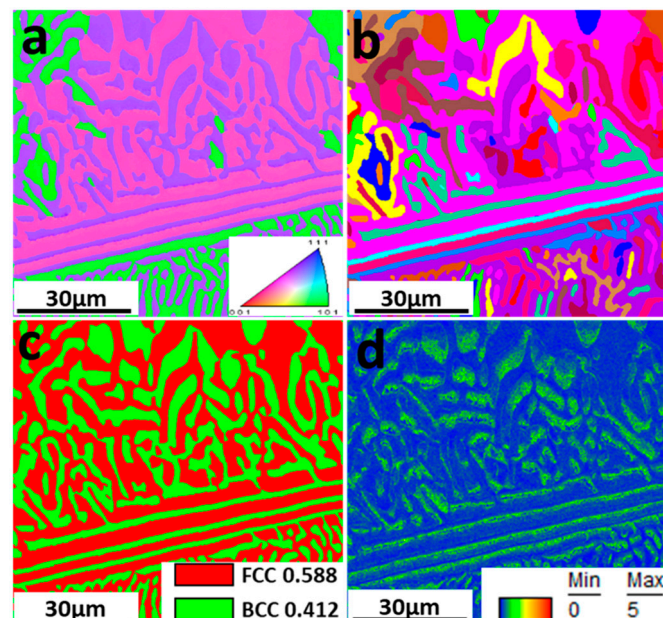


Figure 2. EBSD results of AlCoCrFeNi_{2.1}: (a) IPF map; (b) Grain map; (c) Phase map; (d) KAM map.

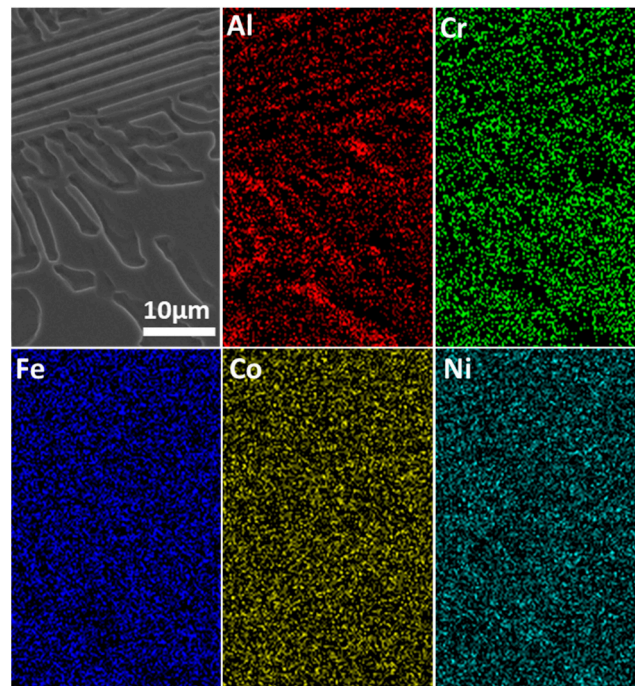


Figure 3. EDS of AlCoCrFeNi_{2.1}.

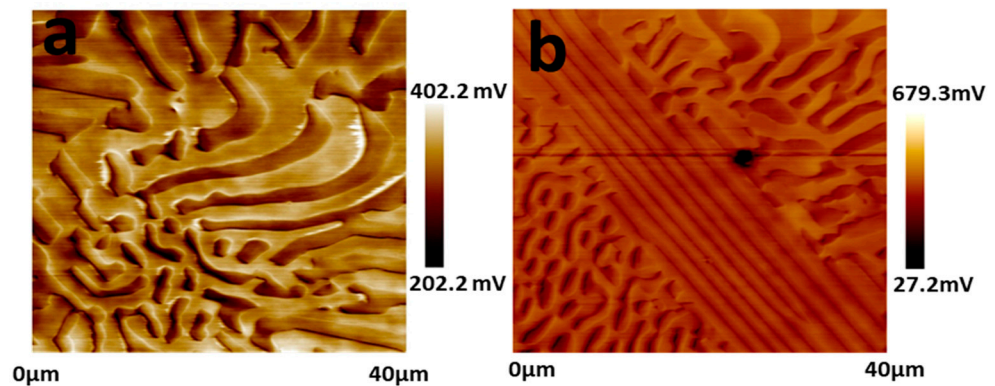


Figure 4. Volta potential mappings of AlCoCrFeNi_{2.1} tested by SKPFM. (a,b) potential map of the irregular region and the lamella region.

3.2. Electrochemical Analysis

Figure 5 presents the potentiodynamic polarization curves and passive current density (i_p) of the AlCoCrFeNi_{2.1} EHEA in the sulfuric acid solution containing chloride. The PDP curves reveal typical passivation characteristics. The curves are composed of active, transition, passive and transpassive regions, which is similar to the electrochemical characteristics of Al-containing HEA and 304 stainless steel [35,36]. The polarization curves shift towards the right with an increase in temperature, implying that temperature accelerates both anodic and cathodic reactions on the electrode. The primary passive potential (E_{pp}) also exhibits no distinct difference at various temperatures, while the primary passive current density (i_{pp}) increases from 8.82×10^{-3} to 9.51×10^{-2} A/cm² as the temperature rises. This indicates that the barrier to passivation increases with temperature. The values of corrosion potentials (E_{corr}) are nearly -0.38 V at various temperatures, suggesting that temperature does not affect the thermodynamic tendency of corrosion. The passivation transition of the EHEAs at different temperatures is located in the zone ranging from -0.38 V to -0.3 V. The pit potential can be selected when the current density is 0.1 mA/cm² Kao et al. [18] established that Cl⁻ reacts with Al to generate metastable ion complexes on Al-containing HEA. A temperature rise stimulates the reaction, which is one of the

reasons for the poor passive capacity of the EHEA at high temperatures. Overall, i_p raises, transpassive potential (E_b) falls, and the passive range becomes narrower with an increase in environmental temperature, indicating that it is more difficult to passivate the alloy, and the passive film is subject to break at high temperature. The results confirmed that an increase in temperature promotes the dissolution of the EHEAs in chloride-containing sulfuric acid solution containing Cl^- . In addition, $\text{AlCoCrFeNi}_{2.1}$ does not possess satisfactory pitting resistance at relatively high environmental temperatures.

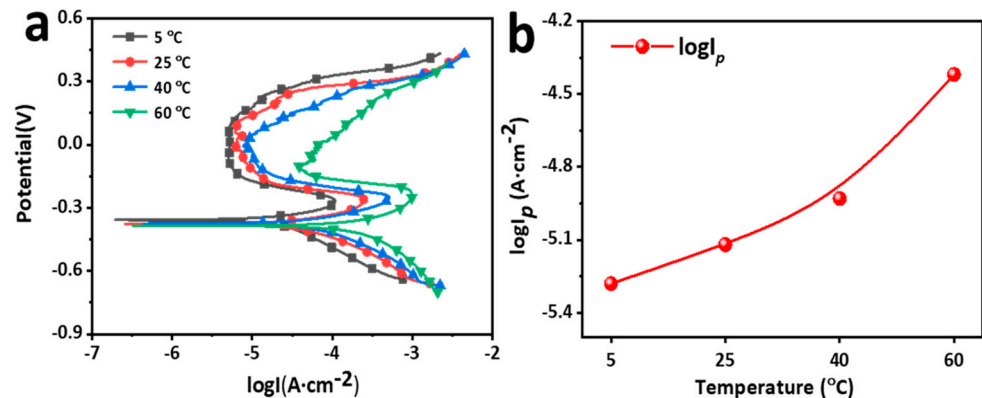


Figure 5. Potentiodynamic polarization curves of $\text{AlCoCrFeNi}_{2.1}$ in chloride-containing sulfuric acid solution at different temperatures: (a) PDP curve; (b) passivity current density.

Electrochemical impedance spectroscopy was employed to study the corrosion behavior of the $\text{AlCoCrFeNi}_{2.1}$ EHEA in the sulfuric acid solution at different temperatures. The Nyquist and Bode plots are shown in Figure 6. The diameter of the semi-arc decreases with the increase in temperature. The Nyquist plot of the EHEA at a temperature of 5 °C exhibits a capacitive loop and an inductive loop at high and low frequencies, respectively. However, the Nyquist plot only shows a capacitive loop at 25 °C and above. The capacitive loop is controlled by the charge transfer process, which is related to the interface reaction. Furthermore, the inductive loop is caused by the relaxation and adsorption of H^+ and Cl^- and the dissolution of the oxide layer and the EHEA [37,38]. In Figure 6b, the impedance at 0.1 Hz revealed the polarization resistance in the solutions, and the impedance with maximum values in the four test temperatures possesses the best corrosion resistance. Figure 6c indicates that the values of the angle fall from 57° to 22° as the temperature from 5 °C to 60 °C. According the Nyquist and Bode plots, the equivalent circuit diagrams in Figure 6e,f are selected to fit the EIS results at 5 °C and other temperatures, respectively. In the graphs, CPE represents the constant phase element of double-layer capacitance, R_s is the solution resistance, R_{ct} denotes the Charge transfer resistance, L represents the inductance, and R_L is the inductance resistor. Due to surface heterogeneity, the capacitance, it is widely accepted that CPE can be applied to replace capacitance in the equivalent circuit diagrams. The impedance of CPE can be described as follows:

$$Z_{CPE} = \frac{1}{Q(j, \omega)^n} \quad (1)$$

where Q represents the magnitude of the CPE , j is an imaginary unit, ω denotes the angular frequency, and n reflects the capacitive character of the CPE . The fitting results are presented in Figure 6d and summarized in Table 1. The errors occur during the fitting process and the error values are calculated by software. Temperature slightly affects the value of n at temperatures from 5 °C to 40 °C, and the n value at a temperature of 60 °C is marginally lower than at other temperatures, implying that the similar charge transfer process on the EHEA surfaces remains similar at temperatures of 5 °C, 25 °C, and 40 °C. The variable R_{ct} is used to evaluate corrosion resistance. The value of R_{ct} decreases sharply with the increase in temperature, since the electrochemical reaction is significantly boosted by the

rising temperatures. The results indicate that there is a good correlation between the PDP and EIS data, which suggests that the corrosion resistance of the AlCoCrFeNi_{2.1} EHEA is unsatisfactory in chloride-containing sulfuric acid solution at higher temperatures.

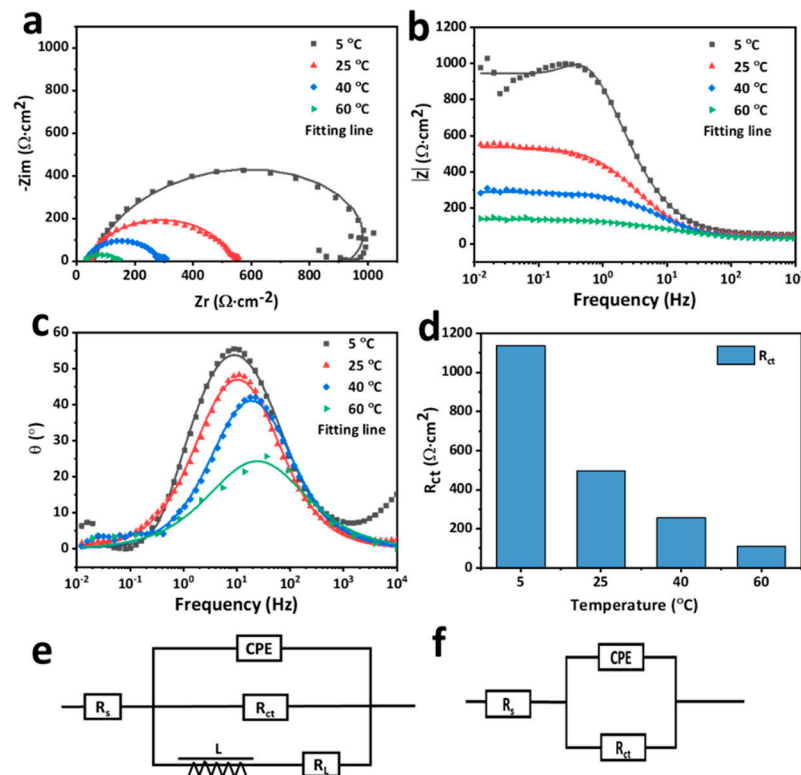


Figure 6. EIS results of AlCoCrFeNi_{2.1} in chloride-containing sulfuric acid solution at different temperatures, (a) Nyquist map; (b) Bode map; (c) Phase map; (d) Fitting results of R_{ct} ; (e) the equivalent electrical circuit at 5 °C; (f) the equivalent electrical circuit at 25 °C, 40 °C, and 60 °C.

Table 1. EIS fitting results of AlCoCrFeNi_{2.1} in the test solution.

Temperature (°C)	R_s ($\Omega \cdot \text{cm}^2$)	Q_{dl} ($\Omega^{-1} \cdot \text{cm}^{-2} \cdot \text{s}^n$)	n	R_{ct} ($\Omega \cdot \text{cm}^2$)	R_L (H cm^2)
5	51.58 ± 1.08	$(1.43 \pm 0.11) \times 10^{-4}$	0.84 ± 0.011	1138 ± 23.9	2195
25	42.78 ± 0.21	$(2.15 \pm 0.04) \times 10^{-4}$	0.84 ± 0.004	495.9 ± 3.07	-
40	32.86 ± 0.23	$(2.27 \pm 0.12) \times 10^{-4}$	0.83 ± 0.006	255.6 ± 1.85	-
60	29.42 ± 0.35	$(6.76 \pm 0.39) \times 10^{-4}$	0.68 ± 0.012	110.1 ± 1.47	-

Potentiostatic polarization is used to characterize the effect of temperature on the passive film of the AlCoCrFeNi_{2.1} EHEA, and the applied potential was $-0.1 V_{vsSCE}$, as Figure 7 shows. Current density drops dramatically in the early stages, which is attributable to the rapid formation of the passive film. Then, it reaches a stable state due to the balance between generation and dissolution of the passive film. Fluctuations in current density in the steady condition increase with temperature, indicating that a leaking passive film with relatively poor protection forms on the EHEA at a higher temperature. The fluctuations of current densities were seen at the end of potentiostatic polarization curves at higher temperatures. Some scholars considered that the fluctuations are related to metastable pitting [39,40].

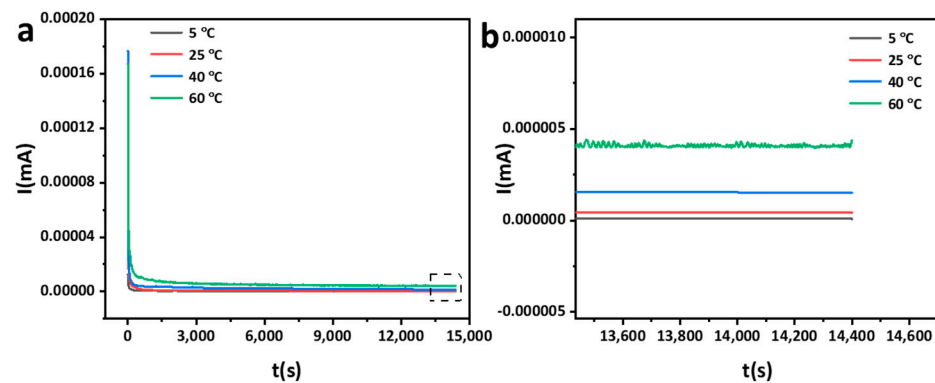


Figure 7. Potentiostatic polarization curves of AlCoCrFeNi_{2.1} in chloride-containing sulfuric acid solution at different temperatures, (a) complete image; (b) enlarged image.

Mott-Schottky curves are used to study the semiconductor properties and density of the charge carriers in passive films. The Mott-Schottky theory presupposes that the Helmholtz capacitance is much higher than the capacitance of the space charge layer. The space charge capacitance for a semiconductor under depletion conditions can be described by Equations (2) and (3):

$$\frac{1}{C_{SC}^2} = \frac{2}{e\epsilon_r\epsilon_0 N_D} \left(E - \varphi_{fb} - \frac{\kappa T}{e} \right) \quad (2)$$

$$\frac{1}{C_{SC}^2} = \frac{2}{e\epsilon_r\epsilon_0 N_A} \left(E - \varphi_{fb} - \frac{\kappa T}{e} \right) \quad (3)$$

where C_{sc} is the space charge capacitance, e represents the electron charge (1.60218×10^{-19} C), E denotes the applied potential, ϵ_r is the dielectric constant of the film, ϵ_0 is the vacuum permittivity (8.85×10^{-14} F/cm), N_D represents the donor density, N_A is acceptor density, φ_{fb} signifies the flat-band potential, κ stands for Boltzmann constant (1.38×10^{-23} J/K), and T is the absolute temperature.

Figure 8 shows the Mott-Schottky curves of the AlCoCrFeNi_{2.1} EHEA after potentiostatic polarization. The curves possess two linear portions with negative and positive slopes at 5 °C and 25 °C, while only positive slopes at 40 °C and 60 °C, implying that the film on the EHEA exhibits the characteristics of a p-n type semiconductor at temperatures of 5 °C and 25 °C and n-type semiconductor at 40 °C and 60 °C. According to conventional wisdom, the outer region of the film, which is composed mainly of Cr oxides, can be considered an n-type semiconductor. In contrast, the inner part of the film consists of Fe oxides and displays p-type semiconductor properties. The negative aspect of the curve shows the electronic feature of a p-type semiconductor, which describes the cation vacancy defect. The linear region with a positive slope reveals that the passive film has the properties of an n-type semiconductor, implying the presence of oxygen vacancies and cation interstitials in the passive film. The semiconductor type is influenced by environmental temperature, which is different from the past reports [26,29]. However, the capacitance value drops noticeably as the temperature increase from 5 °C to 40 °C, while there are minor differences between 40 °C and 60 °C. Changes in hole concentration in the valence are closely related to anion adsorption and result in variations of capacitance value. Fluctuations in capacitance value can be attributed to the electron-depleted layer and charge carriers. Furthermore, the formation of a more disordered passive film at elevated temperatures lead to higher donor density values. The N_D value is obtained from the straight-line portion in the Mott-Schottky curve, as presented in Table 2. Additionally, the variable φ_{fb} presents similar values at different environmental temperatures. The magnitudes of both N_D and N_A are 10^{22} cm⁻³, which is more than the passive film on stainless steel, implying that the film on the EHEA exhibits poor protection. The value of N_D at 5 °C is the lowest, and N_D decreases slightly

as the temperature rises from 25 °C to 60 °C, implying a high solution/metal interface electrochemical reaction at room temperature and above. Passive films with high N_D and N_A values exhibit a certain degree of disorder, and some studies have reported on this influence in the Mott-Schottky curve of metals. Huang et al. [41] stated that the high N_D and N_A values on the passive film of alloy 690 was due to the fast diffusion of metallic ions at high temperature. Cui et al. [29] found that the carrier density of the film on 2057 stainless steel increases with temperature because of the formation rates of oxygen vacancies. According to the point defect model (PDM) devised by Macdonald [42], cation vacancies were generated during the adsorption process of chloride to the active site of oxygen, and a temperature increase enhanced oxygen vacancy formation and anion diffusion. Based on the above findings, although the Fe and Cr content in the film affects the film properties, changes in N_D and N_A not only reveal the defect concentration in the space charge layer, but also demonstrate variation in Fe or Cr oxide. The influence on film composition was analyzed by XPS tests, which revealed that Cl^- transmission is controlled by temperature, affecting the value of N_D and N_A . The AlCoCrFeNi_{2.1} EHEA consists of multiple elements, and the effect of temperature on the electrochemical activity of the different elements varies, which is a critical factor of N_D and N_A . Furthermore, c reflects the ability to repair defects in passive film, and N_D represents the defect density of the passive film. Therefore, there may be an association between i_p and N_D . According to the PDP and M-S results, we have noticed that the N_D shows an exponential relation with $\log i_p$ in chloride-containing sulfuric acid solution at different temperatures, as Figure 9 shows.

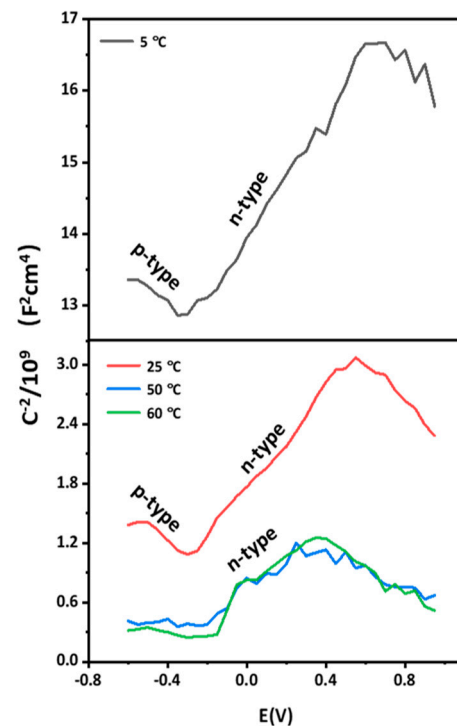


Figure 8. Mott-Schottky curves of the film on AlCoCrFeNi_{2.1} in chloride-containing sulfuric acid solution at different temperatures.

Table 2. N_A and N_D of AlCoCrFeNi_{2.1} in test solution at different temperatures.

Temperature (°C)	N_D ($10^{21} \cdot \text{cm}^{-3}$)	N_A ($10^{22} \cdot \text{cm}^{-3}$)
5	1.2788	7.3417
25	4.2757	7.3643
40	7.6035	-
60	8.8372	-

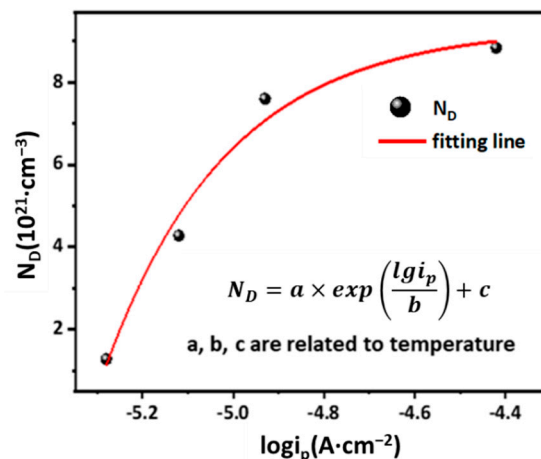


Figure 9. The relationship between N_D and i_p in chloride-containing sulfuric acid solution at different temperatures.

3.3. XPS Analysis

XPS tests were conducted to investigate the influence of temperature on the film composition. Figure 10 shows the spectra of Al 2p, Cr 2p_{3/2}, Fe 2p_{3/2}, Ni 2p_{3/2}, and O 1s after data processing with the XPSpeak 4.1 software. The Al 2p spectra are separated into two peaks representing metallic Al (72.5 eV) and Al₂O₃ (74.7 eV). Due to the slight disparity between the peak of FeO and Fe₂O₃, they are not detected separately in previous literature, and many researchers fitted the Fe spectra based on the valence state [12,43]. However, the Fe spectra can be segmented into four distinct peaks representing Fe²⁺_{ox} (708.4 eV), Fe³⁺_{ox} (710 eV), Fe³⁺_{hy} (711.8 eV) and metallic Fe (706.8 eV). Since FeO is unstable, hence the peak of Fe²⁺_{ox} has been primarily attributed to Fe₃O₄. The intensity of the peaks indicates that Fe³⁺_{ox} and Fe³⁺_{hy} are the primary forms of Fe in the film on the EHEA at both 5 °C and 60 °C. Cr compounds are considered stable in the passive film on passive metals. Figure 10 shows that Cr³⁺_{ox} (576.2 eV), Cr³⁺_{hy} (557.4 eV), and metallic Cr (573.8 eV) appear in the film at 5 °C and 60 °C. The peak intensities of Cr³⁺_{ox} and Cr³⁺_{hy} are very similar at 5 °C, implying that they are the primary constituents of chromium in the film. Nevertheless, Cr³⁺_{hy} is the main component of the film at 60 °C, owing to its higher peak. This indicates that temperature affects the composition of the film. Cr³⁺_{ox} and Cr³⁺_{hy} are identified as the major components in the passive film in many alloys, and Cr₂O₃ contributes to film protection. Combined with the Mott-Schottky curves, we can conclude that the temperature affected the film properties by changing the form of chromium in the film. The Ni 2p_{3/2} component exhibits four peaks representing Ni²⁺_{ox} (856 eV), Ni²⁺_{hy} (853.9 eV), metallic Ni (852.6 eV), and satellite Ni (859.4 eV), which is used for auxiliary analysis. It has been reported that metallic Ni on the film/matrix interface can hinder ion transmission [44]. In addition, a metallic state and low levels of Ni²⁺_{ox} have been observed in the passive film on stainless steel [29,45]. In this study, due to the high content of Ni in the EHEA, various forms of Ni were detected in the film. The intensity of the three peaks is roughly equal at 5 °C and 60 °C, demonstrating that the form of Ni is not influenced by the temperature. The O 1s are dominated by O²⁻, OH⁻, and H₂O. O²⁻ and OH⁻ correspond to the formation of Cr, Al, Ni, and Fe hydroxides and oxides. Furthermore, hydroxide is the primary component in the film in chloride-containing sulfuric acid solution.

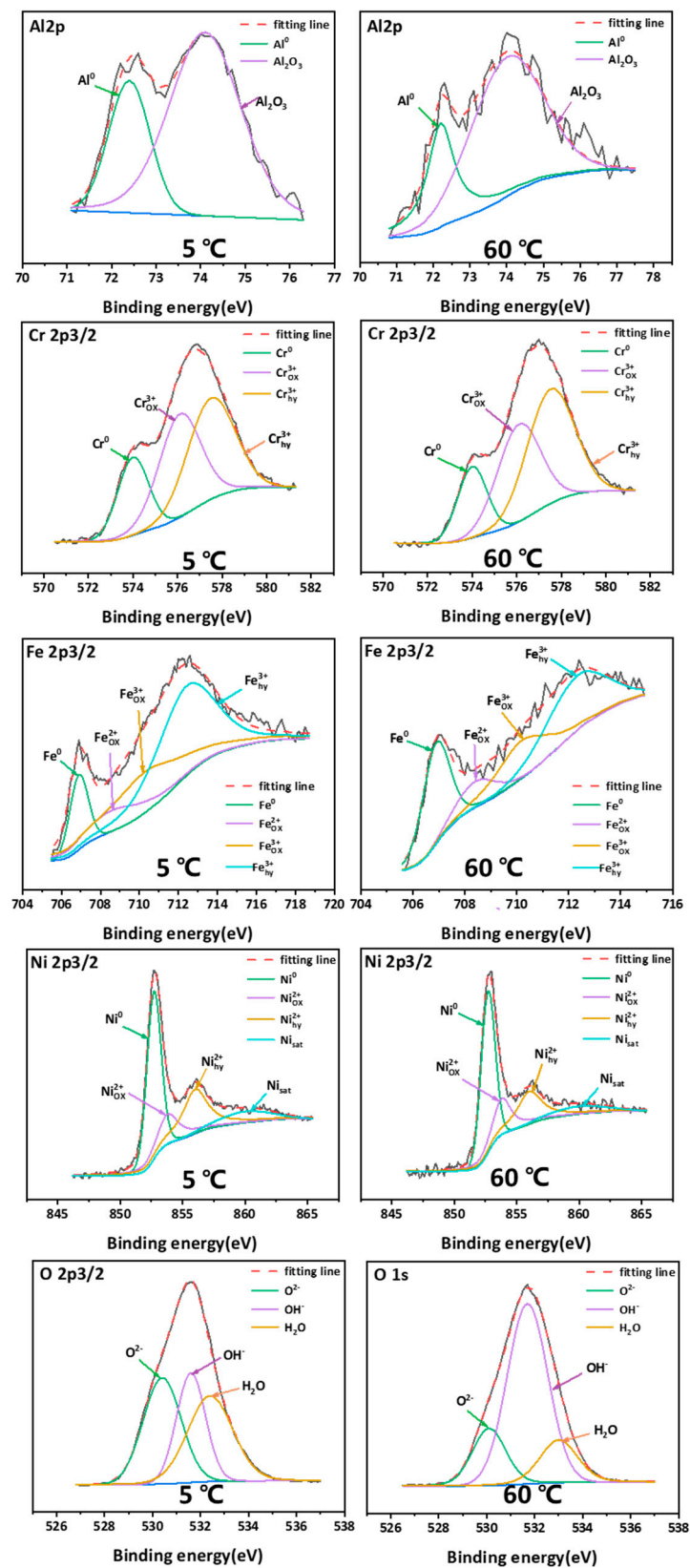


Figure 10. XPS results for Al 2p, Fe 2p_{3/2}, Cr 2p_{3/2}, Ni 2p_{3/2}, and O 1s in the film on AlCoCrFeNi_{2.1} in chloride-containing sulfuric acid solutions at 5 °C and 60 °C.

To further study the effect of temperature on the film of the EHEA, semiquantitative analysis of the XPS data was made using fitting software. Figure 11 displays the percentages

of Al 2p, Fe 2p_{3/2}, Cr 2p_{3/2}, Ni 2p_{3/2}, and O 1s in the test solutions at 5 °C and 60 °C. Al₂O₃ is the main component in the film, and its composition is not affected by temperature. We found that metallic Ni is not the primary form of nickel in the film, while the proportion of oxides and hydroxides is relatively high in the film at tested temperatures. In addition, the ratio of each component was not affected by temperature. An increase in temperature causes a variation in the atomic percentages of the components of Fe 2p_{3/2} and Cr 2p_{3/2}. Furthermore, the O²⁻/OH⁻ ratio of passive film at 5 °C is much higher than at 60 °C, indicating that a more compact film forms in the acidic solution at low temperature. The temperature has a specific influence on the O²⁻/OH⁻ ratios of chromium and iron but does not change the composition of aluminum and nickel. This suggests that the formations of chromium, iron oxide, and iron hydroxide are the primary factors that influence corrosion resistance between low and high temperatures.

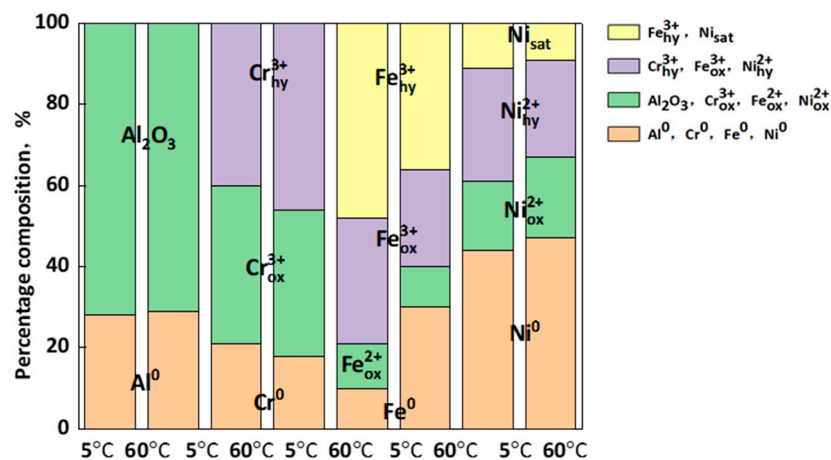


Figure 11. Atomic percentages of the component peaks to the total intensity of Al 2p, Fe 2p_{3/2}, Cr 2p_{3/2}, Ni 2p_{3/2}, and O 1s in the film on AlCoCrFeNi_{2.1} in the acid solutions at 5 °C and 60 °C.

3.4. Corrosion Observation

The corrosion morphologies of the EHEA at various temperatures after potentiostatic polarization for 30 min were observed using SEM, and the results are shown in Figure 12. In general, the temperature has an obvious influence on the corrosion behavior of the EHEA. Corrosion of the EHEA occurs in both regular and irregular patterns and exhibits apparent selectivity. Only the pitting appears at 5 °C, while pitting and few selective dissolution regions are observed at 25 °C. Furthermore, pitting and more selective dissolution zones occur at 40 °C and 60 °C, indicating that an increase in temperature increases the rate of selective dissolution. The distribution of elements around local corrosion was investigated by EDS, as Figure 13 displays. There is almost no aluminum in the pit, a small amount of Ni, and high content of Fe, Cr, and Co. The Al-Ni-rich phases are selectively dissolved. The galvanic effect between the B2 and L12 phase resulted in selective anodic dissolution. This is caused by the heterogeneous distribution of elements and dislocation density (Figures 2 and 3), which is supported by the SKPFM data (Figure 4). It has been previously reported that Al reacts with sulfate radical and hydroxide to generate the chelate compound [18]. The results implied that the Cr-rich phase exhibits better corrosion resistance. Furthermore, the passive film on the Al-Ni-rich phase have a higher Al₂O₃ content than L12 phase, resulting in more defect. Thus, the inside of the B2 phase cannot be identified. Based on the above conclusions, the corrosion process of the EHEA in the test solution is schematically described in Figure 14. The passive films of few Al-Ni-rich phases are attacked by Cl⁻ at lower temperature (Figure 14a2), and then occurs localized corrosion (Figure 14a3); while the passive films of Al-Ni-rich phases are damaged (Figure 14b2), and more Al-Ni-rich phases are dissolved at higher temperature (Figure 14b3). Metastable pits are preferentially created on the grain boundary or B2 phase. Pitting is enhanced by the

effect of polarization. Due to autocatalysis by the caustic ions, the metastable pits gradually grow in the pitting corrosion area or the selective dissolution region. Moreover, the size of the selective dissolution region increases with temperature, and pitting occurs on the surface at various temperatures.

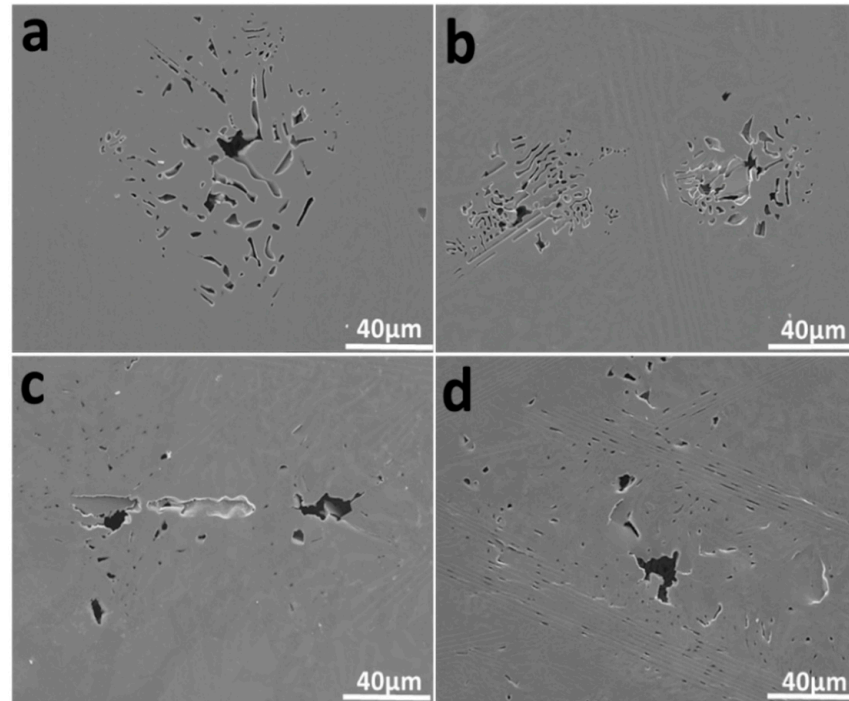


Figure 12. Pitting of AlCoCrFeNi_{2.1} in chloride-containing sulfuric acid solution at: (a) 5 °C; (b) 25 °C; (c) 40 °C; (d) 60 °C.

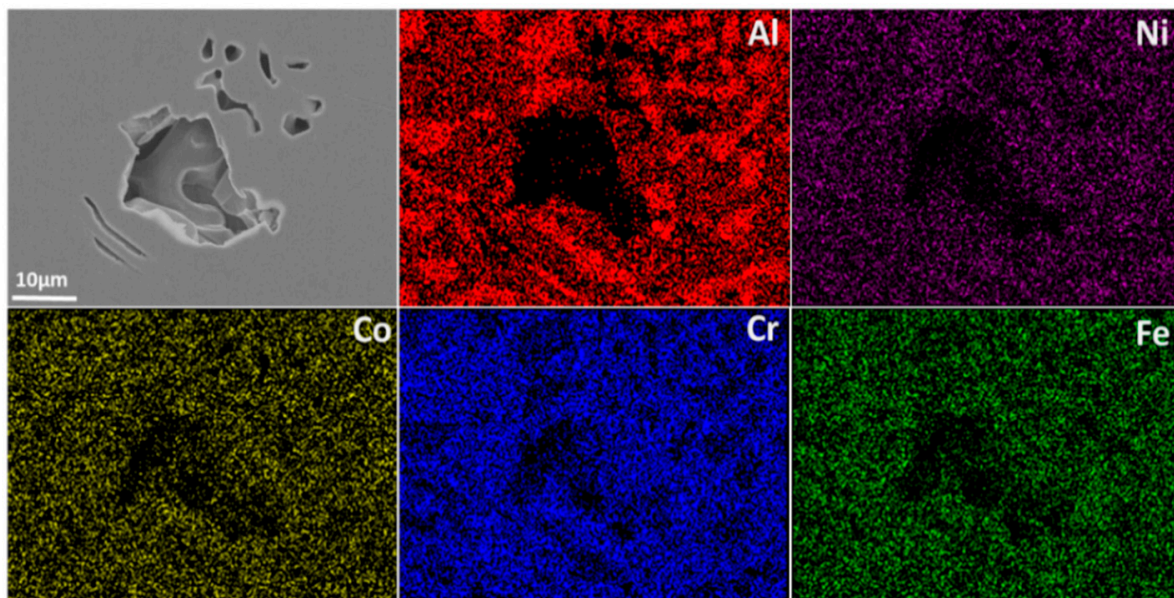


Figure 13. EDS of local corrosion on AlCoCrFeNi_{2.1} in chloride-containing sulfuric acid solution at 5 °C.

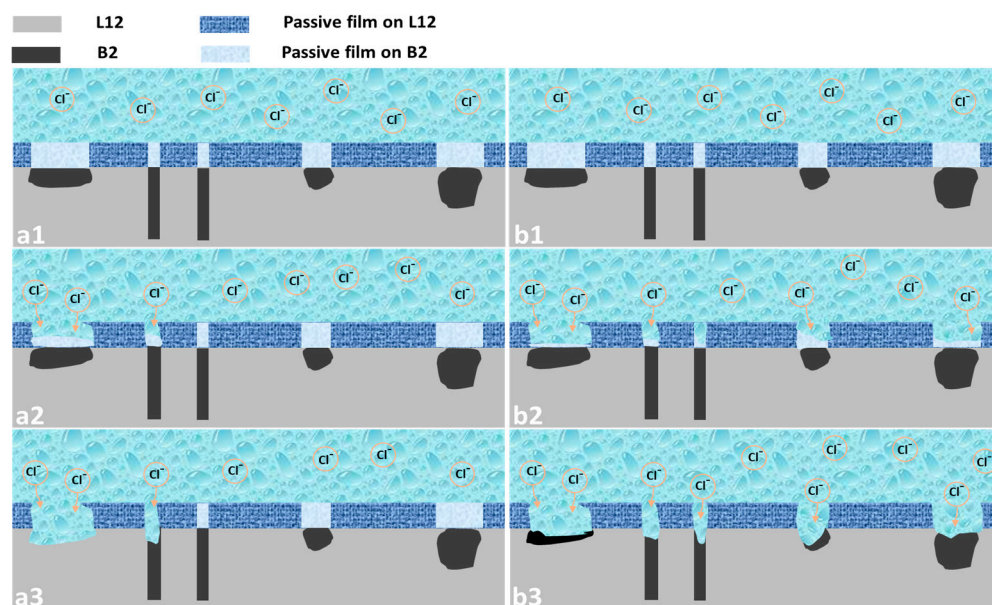


Figure 14. Schematic diagram of corrosion on AlCoCrFeNi_{2.1} in chloride-containing sulfuric acid solution at: (a1–a3) low temperature; (b1–b3) high temperature.

4. Conclusions

The effect of temperature on the passive and corrosion behavior of AlCoCrFeNi_{2.1} EHEA in chloride-containing sulfuric acid solution is studied using electrochemical tests, XPS analysis, and corrosion morphology observation. The main conclusion is as follows:

(1) Based on potentiodynamic polarization curves, the EHEA exhibits an active-passive-transpassive behavior in chloride-containing sulfuric acid solutions at different temperatures. A temperature rise induces a decrease in the transpassive potential and an increase in passive current, and the cathodic reactions are enhanced by the temperature increase.

(2) A change in temperature affect both the semiconductor type and the doping density of the passive film on the EHEA. The passive film on the EHEA consists of hydroxides and oxides of Al, Fe, Cr, and Ni. Temperature variations alter the ratio of the hydroxides and oxides of Fe and Cr but do not have pronounced effect on Al and Ni. The effect of temperature on passive film is determined by variations in the hydroxides and oxides of Fe and Cr, as well as doping density.

(3) Corrosion of the EHEA occurs preferentially in the Al-Ni-rich phase in the chloride-containing sulfuric acid solution at different temperatures. Pitting is the main form of corrosion at low temperatures, while both pitting and selective dissolution occur at a higher temperature. Moreover, rising temperatures promote selective dissolution.

Author Contributions: Conceptualization, L.S. and X.G.; Data curation, L.S.; Investigation, W.H., X.Z., B.L., S.W. and L.K.; Supervision, B.L., S.W., L.K. and X.G.; Resources, L.S. and X.G.; Writing—review and editing, L.S. and X.G. All authors have read and agreed to the published version of the manuscript.

Funding: This work is supported by the Guangdong Basic and Applied Basic Research Foundation (No. 2021A1515110560).

Institutional Review Board Statement: Not applicable.

Informed Consent Statement: Not applicable.

Data Availability Statement: The raw/processed data required to reproduce these findings cannot be shared at this time as the data is related to an ongoing study.

Conflicts of Interest: The authors declare no conflict of interest.

References

1. Cantor, B.; Chang, I.T.H.; Knight, P.; Vincent, A.J.B. Microstructural development in equiatomic multicomponent alloys. *Mater. Sci. Eng. A* **2004**, *375–377*, 213–218. [[CrossRef](#)]
2. Youssef, K.M.; Zaddach, A.J.; Niu, C.; Irving, D.L.; Koch, C.C. A Novel Low-Density, High-Hardness, High-entropy Alloy with Close-packed Single-phase Nanocrystalline Structures. *Mater. Res. Lett.* **2014**, *3*, 95–99. [[CrossRef](#)]
3. Lu, Y.; Dong, Y.; Jiang, H.; Wang, Z.; Cao, Z.; Guo, S.; Wang, T.; Li, T.; Liaw, P.K. Promising properties and future trend of eutectic high entropy alloys. *Scr. Mater.* **2020**, *187*, 202–209. [[CrossRef](#)]
4. Liang, Y.J.; Wang, L.; Wen, Y.; Cheng, B.; Wu, Q.; Cao, T.; Xiao, Q.; Xue, Y.; Sha, G.; Wang, Y.; et al. High-content ductile coherent nanoprecipitates achieve ultrastrong high-entropy alloys. *Nat. Commun.* **2018**, *9*, 4063. [[CrossRef](#)] [[PubMed](#)]
5. Tian, F.; Varga, L.K.; Chen, N.; Shen, J.; Vitos, L. Empirical design of single phase high-entropy alloys with high hardness. *Intermetallics* **2015**, *58*, 1–6. [[CrossRef](#)]
6. Lu, Y.; Dong, Y.; Guo, S.; Jiang, L.; Kang, H.; Wang, T.; Wen, B.; Wang, Z.; Jie, J.; Cao, Z.; et al. A promising new class of high-temperature alloys: Eutectic high-entropy alloys. *Sci. Rep.* **2014**, *4*, 6200. [[CrossRef](#)]
7. Lu, Y.; Gao, X.; Jiang, L.; Chen, Z.; Wang, T.; Jie, J.; Kang, H.; Zhang, Y.; Guo, S.; Ruan, H.; et al. Directly cast bulk eutectic and near-eutectic high entropy alloys with balanced strength and ductility in a wide temperature range. *Acta Mater.* **2017**, *124*, 143–150. [[CrossRef](#)]
8. Hu, M.; Song, K.; Song, W. Dynamic mechanical properties and microstructure evolution of AlCoCrFeNi_{2.1} eutectic high-entropy alloy at different temperatures. *J. Alloys Compd.* **2022**, *892*, 162097. [[CrossRef](#)]
9. Gao, X.; Lu, Y.; Zhang, B.; Liang, N.; Wu, G.; Sha, G.; Liu, J.; Zhao, Y. Microstructural origins of high strength and high ductility in an AlCoCrFeNi_{2.1} eutectic high-entropy alloy. *Acta Mater.* **2017**, *141*, 59–66. [[CrossRef](#)]
10. Huang, L.; Sun, Y.; Chen, N.; Luan, H.; Le, G.; Liu, X.; Ji, Y.; Lu, Y.; Liaw, P.K.; Yang, X.; et al. Simultaneously enhanced strength-ductility of AlCoCrFeNi_{2.1} eutectic high-entropy alloy via additive manufacturing. *Mater. Sci. Eng. A* **2022**, *830*, 142327. [[CrossRef](#)]
11. Laleh, M.; Hughes, A.E.; Xu, W.; Cizek, P.; Tan, M.Y. Unanticipated drastic decline in pitting corrosion resistance of additively manufactured 316L stainless steel after high-temperature post-processing. *Corros. Sci.* **2020**, *165*, 108412. [[CrossRef](#)]
12. Liu, J.; Zhang, T.; Meng, G.; Shao, Y.; Wang, F. Effect of pitting nucleation on critical pitting temperature of 316L stainless steel by nitric acid passivation. *Corros. Sci.* **2015**, *91*, 232–244. [[CrossRef](#)]
13. Pao, L.; Muto, I.; Sugawara, Y. Pitting at inclusions of the equiatomic CoCrFeMnNi alloy and improving corrosion resistance by potentiodynamic polarization in H₂SO₄. *Corros. Sci.* **2021**, *191*, 109748. [[CrossRef](#)]
14. Talebian, M.; Raeissi, K.; Atapour, M.; Fernández-Pérez, B.M.; Betancor-Abreu, A.; Llorente, I.; Fajardo, S.; Salarvand, Z.; Meghdadi, S.; Amirnasr, M.; et al. Pitting corrosion inhibition of 304 stainless steel in NaCl solution by three newly synthesized carboxylic Schiff bases. *Corros. Sci.* **2019**, *160*, 108130. [[CrossRef](#)]
15. Uhlig, H.H. Passivity in metals and alloys. *Corros. Sci.* **1979**, *19*, 777–791. [[CrossRef](#)]
16. Yao, J.; Macdonald, D.D.; Dong, C. Passive film on 2205 duplex stainless steel studied by photo-electrochemistry and ARXPS methods. *Corros. Sci.* **2019**, *146*, 221–232. [[CrossRef](#)]
17. Tong, S.; Che, H.L.; Wang, K.S.; Lei, M.K. Passivation kinetics of a high nitrogen face-centered-cubic phase formed on AISI 304L austenitic stainless steel in borate buffer solutions by photo- and electrochemical methods. *Electrochim. Acta* **2021**, *394*, 139110. [[CrossRef](#)]
18. Kao, Y.-F.; Lee, T.-D.; Chen, S.-K.; Chang, Y.-S. Electrochemical passive properties of Al_xCoCrFeNi (x=0, 0.25, 0.50, 1.00) alloys in sulfuric acids. *Corros. Sci.* **2010**, *52*, 1026–1034. [[CrossRef](#)]
19. Mao, F.; Yao, J.; Zhou, Y.; Dong, C.; Kursten, B.; Macdonald, D.D. Determining the electric-field strength in a passive film via photo-induced electric fields. *Corros. Sci.* **2019**, *154*, 239–245. [[CrossRef](#)]
20. Shi, Y.; Yang, B.; Xie, X.; Brechtel, J.; Dahmen, K.A.; Liaw, P.K. Corrosion of Al CoCrFeNi high-entropy alloys: Al-content and potential scan-rate dependent pitting behavior. *Corros. Sci.* **2017**, *119*, 33–45. [[CrossRef](#)]
21. Chen, Y.Y.; Duval, T.; Hung, U.D.; Yeh, J.W.; Shih, H.C. Microstructure and electrochemical properties of high entropy alloys—a comparison with type-304 stainless steel. *Corros. Sci.* **2005**, *47*, 2257–2279. [[CrossRef](#)]
22. Xu, Z.; Zhang, H.; Du, X.; He, Y.; Luo, H.; Song, G.; Mao, L.; Zhou, T.; Wang, L. Corrosion resistance enhancement of CoCrFeMnNi high-entropy alloy fabricated by additive manufacturing. *Corros. Sci.* **2020**, *177*, 108954. [[CrossRef](#)]
23. Chai, W.; Lu, T.; Pan, Y. Corrosion behaviors of FeCoNiCr (x = 0, 0.5, 1.0) multi-principal element alloys: Role of Cr-induced segregation. *Intermetallics* **2020**, *116*, 106654. [[CrossRef](#)]
24. Lin, C.-M.; Tsai, H.-L. Evolution of microstructure, hardness, and corrosion properties of high-entropy Al_{0.5}CoCrFeNi alloy. *Intermetallics* **2011**, *19*, 288–294. [[CrossRef](#)]
25. Wang, Z.; Feng, Z.; Fan, X.-H.; Zhang, L. Pseudo-passivation mechanism of CoCrFeNiMo_{0.01} high-entropy alloy in H₂S-containing acid solutions. *Corros. Sci.* **2021**, *179*, 109146. [[CrossRef](#)]
26. Luo, H.; Zou, S.; Chen, Y.-H.; Li, Z.; Du, C.; Li, X. Influence of carbon on the corrosion behaviour of interstitial equiatomic CoCrFeMnNi high-entropy alloys in a chlorinated concrete solution. *Corros. Sci.* **2020**, *163*, 108287. [[CrossRef](#)]
27. Chou, Y.L.; Wang, Y.C.; Yeh, J.W.; Shih, H.C. Pitting corrosion of the high-entropy alloy Co_{1.5}CrFeNi_{1.5}Ti_{0.5}Mo_{0.1} in chloride-containing sulphate solutions. *Corros. Sci.* **2010**, *52*, 3481–3491. [[CrossRef](#)]

28. Hou, X.; Ren, Q.; Yang, Y.; Cao, X.; Hu, J.; Zhang, C.; Deng, H.; Yu, D.; Li, K.; Lan, W. Effect of temperature on the electrochemical pitting corrosion behavior of 316L stainless steel in chloride-containing MDEA solution. *J. Nat. Gas. Sci. Eng.* **2021**, *86*, 103718. [[CrossRef](#)]
29. Cui, Z.; Wang, L.; Ni, H.; Hao, W.; Man, C.; Chen, S.; Wang, X.; Liu, Z.; Li, X. Influence of temperature on the electrochemical and passivation behavior of 2507 super duplex stainless steel in simulated desulfurized flue gas condensates. *Corros. Sci.* **2017**, *118*, 31–48. [[CrossRef](#)]
30. Lei, L.; Sun, Y.; Zheng, K.; Wang, X.; He, P.; Liu, Y.; Yao, Q.; Yin, L.; Wan, Y.; Li, J.; et al. A comparative study on the critical pitting criteria of a super ferritic stainless steel at different temperatures in chloride or bromide solution. *Corros. Sci.* **2021**, *183*, 109311. [[CrossRef](#)]
31. Guo, Y.; Su, H.; Zhou, H.; Shen, Z.; Liu, Y.; Zhang, J.; Liu, L.; Fu, H. Unique strength-ductility balance of AlCoCrFeNi_{2.1} eutectic high entropy alloy with ultra-fine duplex microstructure prepared by selective laser melting. *J. Mater. Sci. Technol.* **2022**, *111*, 298–306. [[CrossRef](#)]
32. Miao, J.; Yao, H.; Wang, J.; Lu, Y.; Wang, T.; Li, T. Surface modification for AlCoCrFeNi_{2.1} eutectic high-entropy alloy via laser remelting technology and subsequent aging heat treatment. *J. Alloys. Compd.* **2022**, *894*, 162380. [[CrossRef](#)]
33. Peng, P.; Li, S.; Chen, W.; Xu, Y.; Zhang, X.; Ma, Z.; Wang, J. Phase selection and mechanical properties of directionally solidified AlCoCrFeNi_{2.1} eutectic high-entropy alloy. *J. Alloys. Compd.* **2022**, *898*, 162907. [[CrossRef](#)]
34. Wan, D.; Guan, S.; Wang, D.; Lu, X.; Ma, J. Hydrogen embrittlement of additively manufactured AlCoCrFeNi_{2.1} eutectic high-entropy alloy. *Corros. Sci.* **2022**, *195*, 110007. [[CrossRef](#)]
35. Fu, Y.; Dai, C.; Luo, H.; Li, D.; Du, C.; Li, X. The corrosion behavior and film properties of Al-containing high-entropy alloys in acidic solutions. *Appl. Surf. Sci.* **2021**, *560*, 149854. [[CrossRef](#)]
36. Rahimi Kashani, F.; Rezaei, M. Electrochemical studies and molecular simulations on the use of molybdic acid for stabilization of AISI 304 stainless steel passive film in sulfuric acid medium. *J. Mol. Liq.* **2021**, *344*, 117733. [[CrossRef](#)]
37. Cen, H.; Zhang, X.; Zhao, L.; Chen, Z.; Guo, X. Carbon dots as effective corrosion inhibitor for 5052 aluminium alloy in 0.1 M HCl solution. *Corros. Sci.* **2019**, *161*, 108197. [[CrossRef](#)]
38. Abd El Rehim, S.S.; Hassan, H.H.; Amin, M.A. Corrosion inhibition study of pure Al and some of its alloys in 1.0 M HCl solution by impedance technique. *Corros. Sci.* **2004**, *46*, 5–25. [[CrossRef](#)]
39. Qiao, Y.X.; Zheng, Y.G.; Ke, W.; Okafor, P.C. Electrochemical behaviour of high nitrogen stainless steel in acidic solutions. *Corros. Sci.* **2009**, *51*, 979–986. [[CrossRef](#)]
40. Escrivà-Cerdán, C.; Blasco-Tamarit, E.; García-García, D.M.; García-Antón, J.; Akid, R.; Walton, J. Effect of temperature on passive film formation of UNS N08031 Cr–Ni alloy in phosphoric acid contaminated with different aggressive anions. *Electrochim. Acta* **2013**, *111*, 552–561. [[CrossRef](#)]
41. Huang, J.; Wu, X.; Han, E.-H. Electrochemical properties and growth mechanism of passive films on Alloy 690 in high-temperature alkaline environments. *Corros. Sci.* **2010**, *52*, 3444–3452. [[CrossRef](#)]
42. Macdonald, D.D. The history of the Point Defect Model for the passive state: A brief review of film growth aspects. *Electrochim. Acta* **2011**, *56*, 1761–1772. [[CrossRef](#)]
43. Cui, Z.; Chen, S.; Dou, Y.; Han, S.; Wang, L.; Man, C.; Wang, X.; Chen, S.; Cheng, Y.F.; Li, X. Passivation behavior and surface chemistry of 2507 super duplex stainless steel in artificial seawater: Influence of dissolved oxygen and pH. *Corros. Sci.* **2019**, *150*, 218–234. [[CrossRef](#)]
44. Olsson, C.O.A.; Landolt, D. Passive films on stainless steels—chemistry, structure and growth. *Electrochim. Acta* **2003**, *48*, 1093–1104. [[CrossRef](#)]
45. Kocijan, A.; Donik, Č.; Jenko, M. Electrochemical and XPS studies of the passive film formed on stainless steels in borate buffer and chloride solutions. *Corros. Sci.* **2007**, *49*, 2083–2098. [[CrossRef](#)]